Nanoelectronics and Its New Materials – A NEW ERA OF NANOSCIENCE

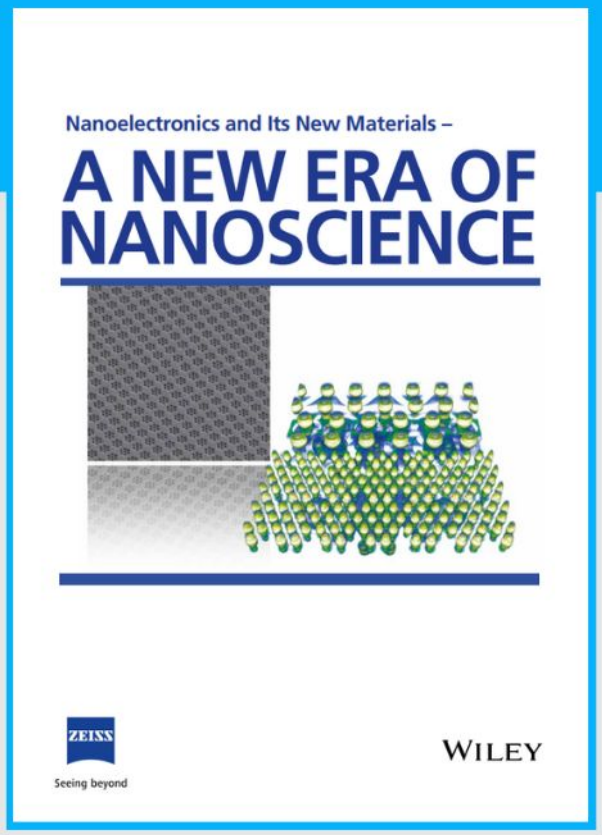

Discover the recent advances in electronics research and fundamental nanoscience.

Nanotechnology has become the driving force behind breakthroughs in engineering, materials science, physics, chemistry, and biological sciences. In this compendium, we delve into a wide range of novel applications that highlight recent advances in electronics research and fundamental nanoscience. From surface analysis and defect detection to tailored optical functionality and transparent nanowire electrodes, this eBook covers key topics that will revolutionize the future of electronics.

To get your hands on this valuable resource and unleash the power of nanotechnology, simply download the eBook now. Stay ahead of the curve and embrace the future of electronics with nanoscience as your guide.

ZEISS

Seeing beyond

WILEY

ADVANCED FUNCTIONAL MATERIALS
www.afm-journal.de

Liquid Metal-Based Sensor Skin Enabling Haptic Perception of Softness

*Haotian Chen, Ivan Furfaro, Emilio Fernández Lavado, and Stéphanie P. Lacour**

Haptic perception of softness is a unique feature of the human skin that relies on the concurrent measurements of the lateral deformation and compression of the skin during object manipulation. This is challenging to implement in robotics because of combined requirements in sensing modalities, skin format, robotic structures, and synthetic materials. A soft sensory skin supporting distributed and bimodal mechanical sensing over large surface area and suitable for robotic hand manipulation is reported. Resistive pressure and strain sensors are prepared with spray-coated liquid metal films embedded in a silicone matrix. Object softness is computed through a calibrated model based on both sensor response curves and the stiffness of the carrier robot. The soft sensory skin enables localization and discrimination of softness that promise interesting future implementation for robotic palpation or precise teleoperation.

1. Introduction

One of the distinctive functions of human skin is its ability to perceive the physical attributes of the external environment through tactile examination. When an object is touched, various mechanoreceptors located within the skin generate diverse perceptual sensations, including softness, fine and coarse roughness, friction, and warmth.[1,2] Softness is particularly valuable for exploring the internal properties of an object, as the softness of a material relates to its ability to deform under pressure. Medical palpation serves as a prime example, wherein physicians can detect and diagnose inflammation or other medical conditions by applying gentle strokes to gauge the softness of the human body.[3] The human capacity to discriminate the softness of an object is the result of combining cutaneous and kinesthetic cues, which rely on tactile inputs from skin mechanoreceptors and manipulation (such as poking or stroking) of the object (**Figure 1**a, left). Recent studies indicate that cutaneous cues become predominant when the touched objects are as soft as or softer than human skin.[4–7]

Currently, researchers are striving to equip robots with this unique human function,[8,9] enabling them to intelligently collaborate with us, particularly in fields like medical applications,[10–12] smart prostheses,[13,14] and human–machine interaction.[15,16] Although current robot technology can obtain kinesthetic information by controlling motors at the joints, the incorporation of cutaneous cues in robots remains a challenge primarily due to the use of rigid materials in traditional robot construction. When they make contact with an unfamiliar object, the traditional robots' rigid materials do not deform significantly as a human finger would as depicted in Figure 1a (right). Since the deformation is so minimal, there is no corresponding sensor to detect it in traditional robot configurations. However, detecting surface deformation is an elementary function of the human cutaneous functions. The human hand would lose plenty of crucial haptic functions if the surface deformation perception is missing, and the same is true for robotic sensing. Therefore, a larger deformation and corresponding sensing technologies are expected in the next-generation robotic cutaneous perception.

The introduction of novel materials[17–19] and advanced fabrication techniques[20–22] have fostered the development of electronic skins, which exhibit promising biomedical applications.[23,24] These electronic skins consist of artificial sensor systems capable of emulating human skin properties, particularly its softness, while monitoring essential data such as strain,[15,25] pressure,[26,27] temperature,[28,29] and humidity.[30,31] In recent years, the focus in this field has shifted from classical single function sensors to multifunctional sensor systems,[32,33] leveraging data fusion algorithms to provide more meaningful insights. For example, the compliance of an object ($c = \delta/F$) can be computed by measuring both the applied force (F) and the resulting displacement (δ) experienced by the object in either mechanical way[34,35] or optical way.[36] However, the creation of a soft compliance sensor system entails more than a simple combination of pressure and strain sensors. The interaction between the sensor and the object, particularly concerning their material properties, is often overlooked. Specifically, most soft pressure sensors operate on resistive or capacitive principles, and changes in resistance or capacitance stem from geometrical alterations. To better clarify this problem, the model of springs in series could help. The

H. Chen, I. Furfaro, E. Fernández Lavado, S. P. Lacour
EPFL Neuro-X Institute Laboratory for Soft Bioelectronic Interfaces
Campus Biotech B3.2
Chemin des mines 9, Geneva 1202, Switzerland
E-mail: stephanie.lacour@epfl.ch

The ORCID identification number(s) for the author(s) of this article can be found under https://doi.org/10.1002/adfm.202308698

DOI: 10.1002/adfm.202308698

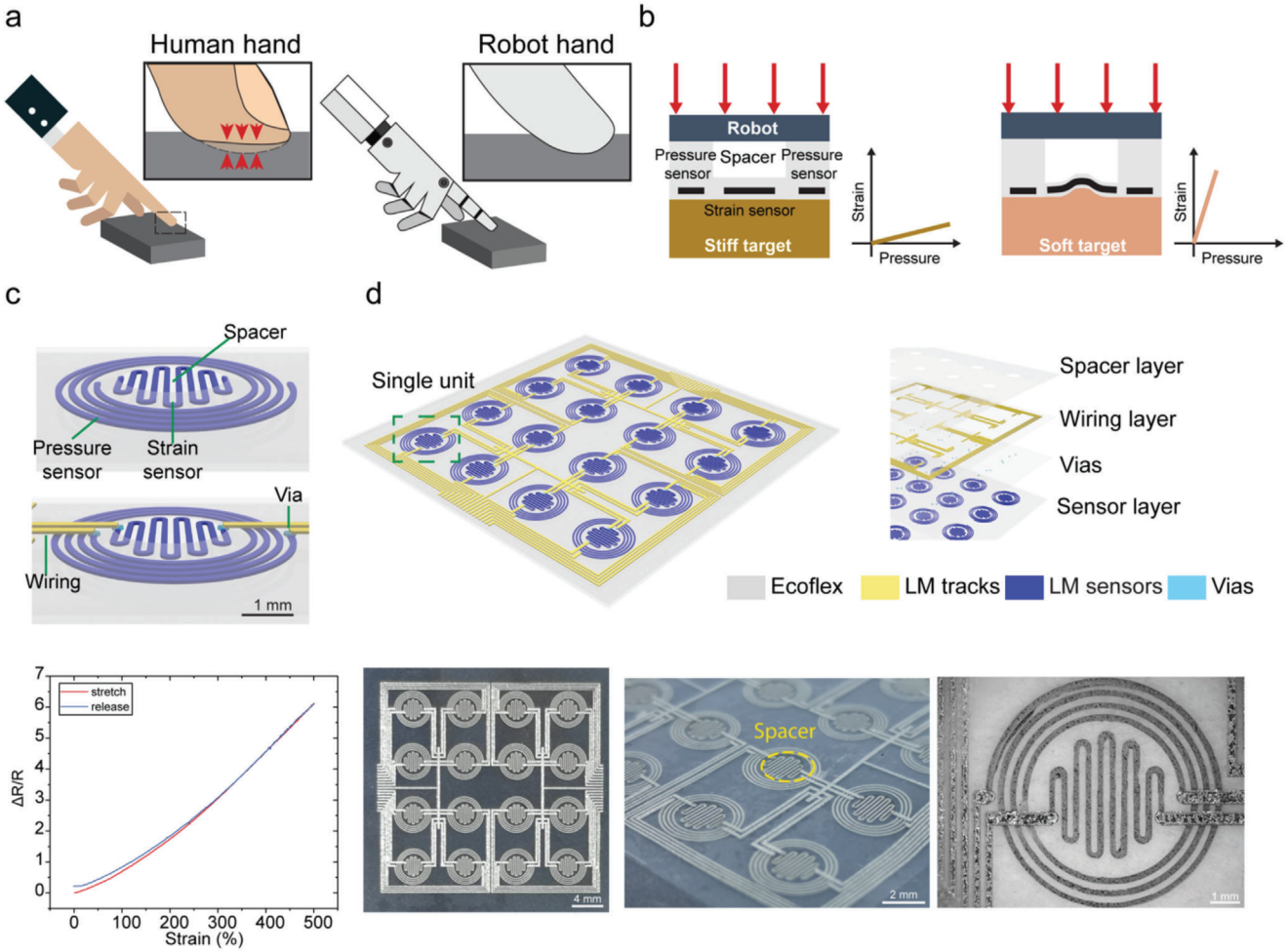

Figure 1. Compliance bimodal sensor system. a) Schematics illustrating the deformation of human and robotic skin upon touch. b) Cross-sections of the proposed compliant sensor system when in contact with a stiff and soft object target. c) Layout of the pressure and strain sensor unit and interconnects. d) Sensor matrix (4 × 4 units) with corresponding layers. e) Relative electrical change as a function of strain of Ecoflex encapsulated EGaIn conductor (width = 0.2 mm, length = 20 mm, R_0 = 12.42, 6 samples). f–h) Optical photographs of the e) sensor matrix, f) wiring, and g) vias.

sensor's stiffness and deformation are defined as k_1, X_1, respectively, while k_2, X_2 are defined as the target object's stiffness and deformation, respectively. The total external compression displacement is $X_{\text{total}} = X_1 + X_2$.

k_1 is known if the sensor's materials and structure are determined. X_1 is directly related to the sensor's readout. Under the prescribed displacement X_{total}, the force on the sensor and the target are the same:

$$X_1 k_1 = X_2 k_2 \tag{1}$$

By putting Equation (1) into X_{total}, we can obtain the following expression:

$$X_1 = \frac{k_2}{k_1 + k_2} X_{\text{total}} \tag{2}$$

Though X_{total} and k_1 are known, the unknown k_2 will influence X_1.

In the case of rigid target materials ($k_2 \gg k_1$), the sensor undergoes substantial deformation, leading to changes in electrical parameters, while the contacted object experiences negligible deformation. This is the most common case when characterizing soft pressure sensors, the latter being usually placed on a rigid testing platform. When the target object is softer than the sensor material ($k_1 \gg k_2$), the situation is reversed: the object undergoes more significant deformation than the sensing module. Consequently, even under the same external compression displacement, the deformation of the sensor depends entirely on the Young's modulus of the target object, potentially introducing significant errors in the measurement and impeding accurate characterization of compliance. Previous research has not adequately addressed this issue, as sensor applications typically involve clear and specific scenarios where the softness of the material being touched is nearly predetermined.

In this study, we present a soft compliance sensor array that aim to mimic the perception of compliance by the human. The array consists of bimodal sensing units made of resistive, strain, and pressure sensors—fabricated using eutectic

gallium indium (EGaIn) liquid metal embedded in elastomer membranes (Ecoflex, Smooth-on, Inc.). To address the issue of the sensor–object softness interaction, we conduct numerical simulations and propose an analytical model to help calibrate accurately the pressure sensor accounting for outputs of the strain sensor. This allows both sensors to operate synergistically thereby enabling accurate computation of compliance. The soft sensors correctly distinguish the compliance of objects made of common soft materials such as rubber and hydrogel but also biological tissues such as chicken heart and breast. We further illustrate the potential of the soft sensing technology in implementing a sensor matrix hosting 16 EGaIn bimodal sensing units to register location, contact area, and compliance of the manipulated object.

2. Design and Working Principle of Bimodal Compliance Sensors

2.1. Layout of the Pressure–Strain Sensor Units

We designed a simple bimodal pressure–strain sensor system to monitor simultaneously applied force and deformation. Both sensors are resistive and embedded in a soft elastomeric membrane. The compliance sensing operation is described in Figure 1b: the sensor system is to be mounted on a rigid structure such as a traditional robotic finger and the objects to be detected are assumed to have a flat, smooth surface, at least at the scale of the sensor system. The pressure sensor detects the applied normal load as the sensing unit touches the target object. The central strain sensor deflects along tangential directions upon contact with the object. The combined outputs of the sensors inform on the object compliance. In the case of a rigid object, the deformation of the pressure sensor predominates while that of the strain sensor is maximal when interfacing a soft, deformable object. By comparing the ratio of the outputs from the strain sensor and pressure sensor, which represent deformation and force, respectively, the compliance of the target object can then be inferred.

Figure 1c displays the schematic of a single bimodal sensing unit. It contains a spiral-shaped pressure sensor, and a meander strain sensor patterned in the center of the spiral. Both resistive sensors are made of liquid metal (LM) spray-coated on the elastomer substrate (Ecoflex). Compared to the methods such as direct writing and printing, spray coating enables a scalable (up to A4/letter paper) production with one step. While in comparison of transfer printing and evaporation, spray coating saves the steps in the cleanroom but with acceptable pattern resolution (up to 20 μm). More information about resolution of liquid metal spray-coating technique can be found in Figure S8 in the Supporting Information.

The thickness of deposited liquid metal can be controlled by the air pressure, nozzle moving speed, and the distance between the nozzle and the substrate. In our work, the thickness of the liquid metal is 20 μm with sheet resistance of 0.15 $\Omega\ \mathrm{sq}^{-1}$. These sensors lay under a spacer layer patterned with holes enabling the deformation of the strain sensor when the unit makes contact with an object.

This design combines the strain sensor and pressure sensor in a compact area, however, comes with the cost of increased difficulty in wiring them in the same plane. Thanks to the liquid metal spray-coating technique, we developed a double-sided LM patterning (DSLM) technique to fabricate liquid metal vias in a fast, efficient, and reliable way, thus greatly facilitating interconnect routing. The sensing and wiring layers are prepared on two different silicone surfaces and connected by liquid metal vias (Figure 1c,d). The detailed fabrication process can be found in the Experimental Section and Figure S1 in the Supporting Information. Spray coating and DSLM make double layer LM electronics possible, extending the patterning from single plane to double side, which greatly enhances the integration of the liquid metal-based soft electronic system.

The spray-coated liquid metal exhibits steady linear electromechanical characteristics under large elongation (0–500% applied strain) with a gauge factor of 1.22 (Figure 1e). According to Figure S2 in the Supporting Information, the soft liquid metal reaches stable electromechanical response after five stretching cycles and sustains a stable response within 1000 cycles. Although the large strain in the electromechanical test is not necessary in the current application, the elasticity of the spray-coated liquid metal on Ecoflex ensures safe handling and manipulation along with stable electrical conduction.

Figure 1f–h illustrates a 4 × 4 sensor matrix and close-ups to individual sensing unit. The overall size of the sensor unit is selected to match human fingertip. The sensors are located in the neutral layer of the whole structure to avoid the strain caused by bending. The outer radius and inner radius of the pressure sensor are 3.9 and 2.5 mm, respectively, while the strain sensor's outer contour is 2.3 mm radius circle. All LM tracks have the same width of 200 μm and the radius of the hole in the spacer layer is 1.8 mm. We can clearly see from Figure 1g that the sensing and wiring layers are in different planes and are connected at the desired positions through the LM filled vias.

2.2. Finite Element Modeling

We modeled the bimodal sensor unit using finite elements to assess the effect of the overall sensor geometry and materials on its output. We defined three critical geometrical parameters (**Figure 2**a): l_p, l_s, t_s the width of the pressure sensor ring, the radius of the strain sensor region, and the thickness of the sensors' membrane, respectively. We define E_s and E_t as the Young's modulus of the sensor carrier material and the target object, respectively.

The sensor unit is mounted on a stainless-steel carrier (mimicking a robotic finger) of 2 cm radius and >10 mm thickness. The target object with thickness of >10 mm can be considered semi-infinite compared to the soft sensor system (thinness <2 mm) (Figure S3, Supporting Information). The sensor geometry, namely, l_s and l_p, is optimized to guarantee maximal output from both sensors and highest sensitivity to compliance (Figure S4, Supporting Information). $l_s = l_p$ is selected for all subsequent experiments.

Figure 2b illustrates resulting displacement maps of the sensor unit when a 1 kPa pressure is applied perpendicularly to a soft (E_t = 100 kPa) or stiff (E_t = 100 MPa) flat object. The central strain sensor deflects significantly when in contact with a soft object compared to a rigid one, confirming the working principle outlined above.

Manufacturing the soft sensor unit with soft materials (E_s< 1 MPa) increases the sensing resolution of both strain

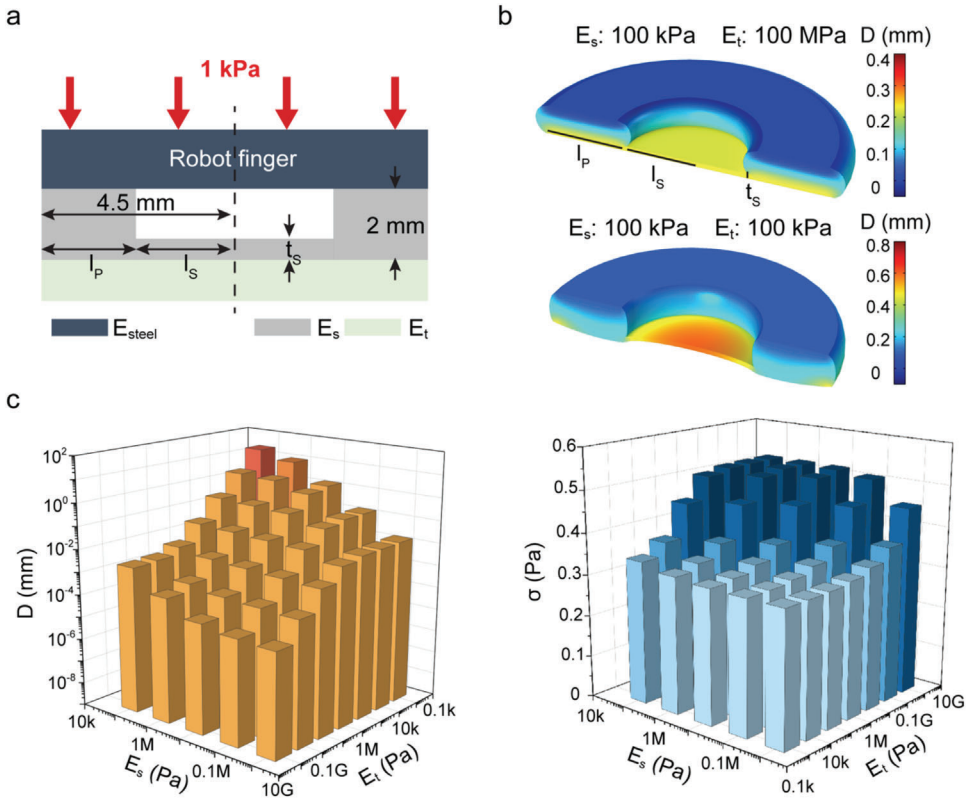

Figure 2. Model of the compliant bimodal sensor unit. a) Schematic cross-section. b) Displacement maps when the sensor unit is touching a stiff (100 MPa) and a soft object (100 kPa). The sensor is prepared with a 100 kPa modulus material. c) Effect of object and sensor stiffness on the outputs of the strain and pressure sensors.

and pressure modalities compared to stiffer carrier materials (Figure 2b,c). For a given sensor carrier, the output of both sensors depends on the stiffness of the target object. For the strain sensor, the resulting deformation increases with the softness of the target material (lower E_t). For the pressure sensor, the resulting compression is the highest with a stiff object (higher E_t).

The sensitivity of the soft sensors is quantified as the slope of their response curves. The highest sensitivity for the strain sensor is observed when the modulus of the target material is near that of the sensor material (Figure S5, Supporting Information). For example, when the sensor system is prepared with an E_s = 100 kPa material, its sensitivity reaches 0.46 mm Pa^{-1} in the 1 kPa to 10 MPa range. However, if the target material is stiff (E_t > 10MPa), the sensor sensitivity decreases to about 0.15 mm Pa^{-1} in logarithmic scale (Figure 2c left and Figure S5a, Supporting Information). Using a stiffer sensor material, e.g., E_s = 100 MPa, reduces the sensitivity of the strain sensor.

When the sensor system is made of hard materials (e.g., E_s = 10 GPa), the resulting stress distribution on its surface is uniform when touching an object with softer modulus (1 kPa < E_t < 10 MPa) (Figure 2c right and Figure S5b, Supporting Information), which infers a lower resolution in distinguishing them. Conversely, when the sensor itself is prepared with a soft material (E_s = 100 kPa), the effect of the target material, especially in the similar range of the sensor material, compliance on the stress distribution comes to the fore.

The nature of the contact between the target material and sensor material is rarely considered as industrial/commercial sensors are usually fabricated with rigid materials. The target objects are typically softer and do not affect the resulting stress distribution. However, with the development of stretchable electronic devices and their interfaces with soft matter such as human body, the characteristics of the materials in contact with them therefore become an essential factor to account for.

3. Results and Discussion

3.1. Calibration of Compliance Measurements

Figure 3a presents a schematic of the experimental set up. The sensor unit is attached to an electromechanical universal test system (MTS Criterion Series 40) to simulate its operation when mounted on a rigid robotic finger. The object to be tested is placed below the sensor on a static platform; the object surface area is typically larger than that of the sensor unit. Applied force and displacement are monitored in real-time. Four object materials are evaluated: commercial rubber (CR, Läufer & Gutenberg GmbH), polydimethylsiloxane (PDMS, Sylgard 184, Dow Corning), Ecoflex (Ecoflex, Smooth-on, Inc.), and hydrogel (agarose based) and modeled in 10 mm radius, 10 mm thickness cylinders. To protect the sample, the applied force is limited within 6 N.

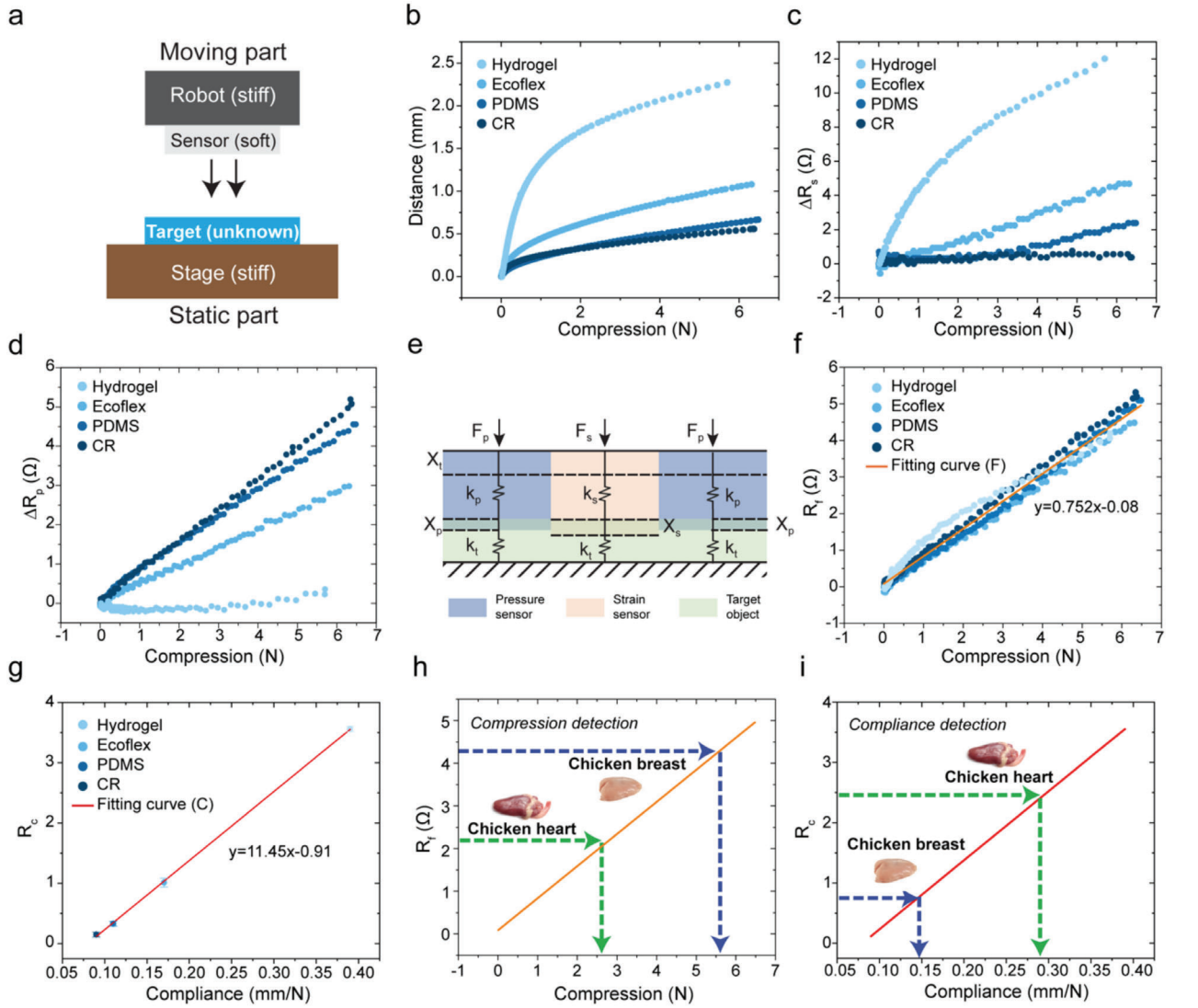

Figure 3. Characterization of the compliant sensor unit. a) Schematic of the experimental set up. b) Tensile response of test materials. c,d) Output (ΔR) of c) the strain R_s and d) pressure R_p sensors when in contact with cylinders of known materials. e) Simplified mechanical model. f) Calibrated sensor output as a function of applied external compression. g) Multimodal response to compliance, $R_c = R_s/R_f$ for distinct materials. h,i) Sensors output and compliance computed upon contact with biological tissues.

Typical force–displacement curves for the four materials are presented in Figure 3b clearly illustrating their softness range. The corresponding outputs of the sensors are shown in Figure 3c,d. As previously discussed, the two sensors display opposite response to softness: the strain (pressure) sensor output is maximal (minimal) when in contact with the softest material, respectively. We derive a simple mechanical model to integrate their combined outputs (Figure 3e) and account for the stiffness of the sensor and object materials. We define k_p, k_s, k_t as the sensor, spacer, and object stiffnesses, respectively.

In order to rule out the measurement error caused by the sensor–object softness interaction, we define R_f as the bimodal sensor output, function of R_s and R_p ($R_f = R_p + 0.32\ R_s$, Supporting Information, Mechanical model, and Figure S6, Supporting Information) and independent on the compliance of the target object (Figure 3f). This enables the quantification of applied load whatever the nature of the material touched by the artificial sensor. Once the total load is known, compliance can be calculated by comparing the ratio of the deformation and the external load, which correspond to the readout from the strain sensor R_s and the calibrated value R_f. We define R_c as $R_c = R_s/R_f$ to illustrate the resulting compliance (Figure 3g). R_c is indeed independent of the applied load and informs on the compliance (Figure S7, Supporting Information).

3.2. Compliance Detection of Biological Tissues

Next, we tested the bimodal sensor unit to probe biological tissues, e.g., chicken breast and heart. Pieces of tissue were positioned on the stage of the MTS and compressed by a 5 mm displacement; the soft senor unit was mounted on the top plate of

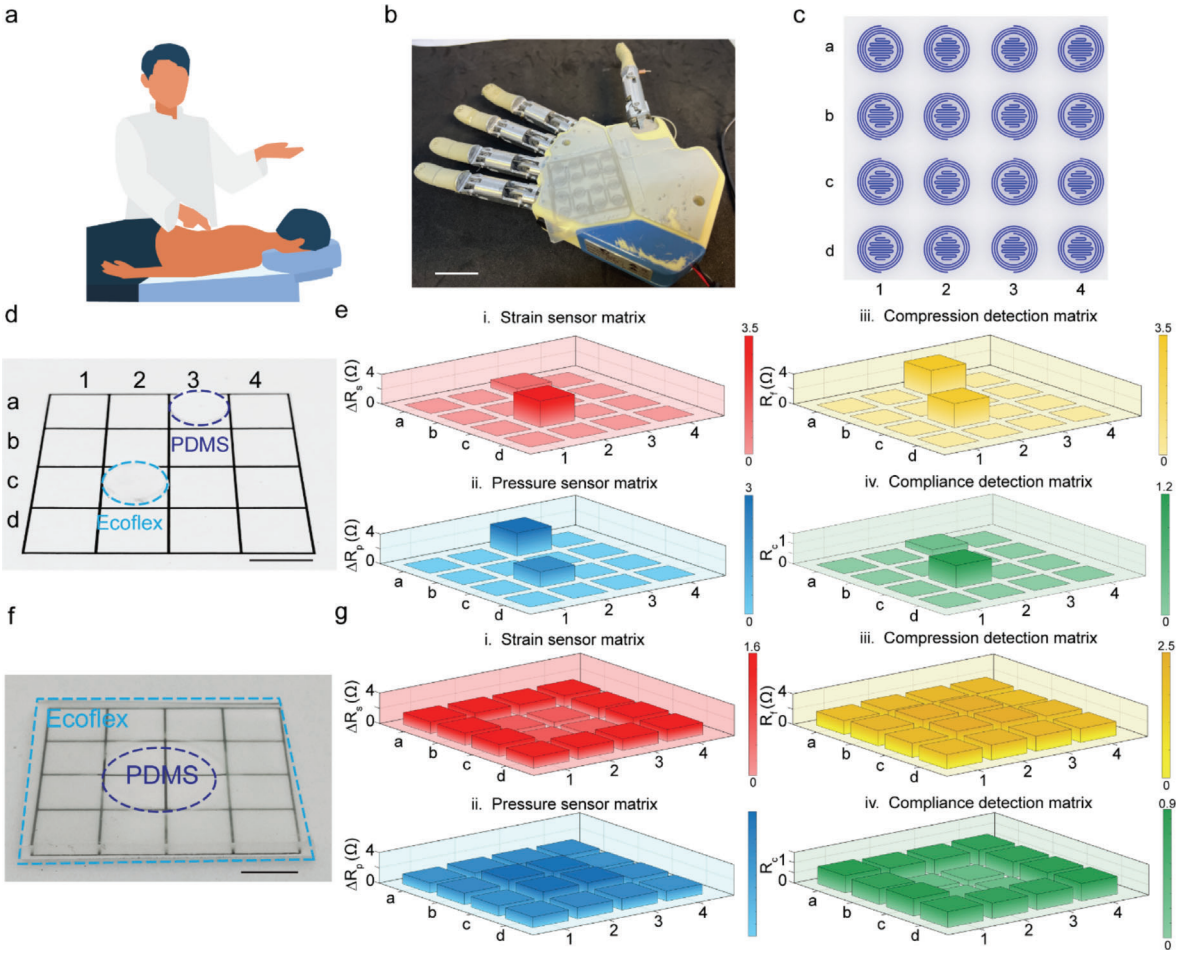

Figure 4. Compliance mapping. a) Schematic of physician palpation. b) Optical image of a 4 × 4 compliance array on the palm of a robotic hand. c) Skin sensor labels. d) Photograph of two objects in contact with the compliance sensor matrix. Both are 1.1 cm diameter, 0.8 mm thick cylinders, one is prepared with PDMS, the other one with Ecoflex. e) Corresponding sensor outputs and detected compliance. f) The object in contact with the soft compliance sensor system is a membrane (4.5 cm side) of Ecoflex within which a cylinder of PDMS (2.2 cm diameter) is embedded. g) Corresponding sensor outputs and detected compliance.

the MTS, in direct contact with the biological tissue. In the case of chicken heart, R_s = 5.02 Ω and R_p = 0.46 Ω. For the chicken breast, R_s = 3.27 Ω and R_p = 3.25 Ω. Based on the calibration described above, the computed compliance is 0.29 and 0.15 mm N^{-1} for the chicken heart and breast, respectively, nicely distinguishing the two muscle tissues.

3.3. Implementation in a Large-Area Sensor Matrix

Palpation relies on touch, pressing and feeling the area being examined (**Figure 4**a), and informs on the size, contour, hardness, etc., of the body surface and organs. However, this effective technique often relies on the experience of the physician as no quantitative systems currently provide accurate information. A single sensing unit is not enough to inform on a large object and/or objects with distinct local compliance. We designed a 4 × 4 sensing matrix to fit the size of the human or robotic palm (Figure 4b) and achieve compliance mapping. The matrix is labeled with a, b, c, d rows and 1, 2, 3, 4 columns (Figure 4c).

We followed two different scenarios. First, one PDMS cylinder and one Ecoflex cylinder with the same radius of 1.1 cm and thickness of 0.8 mm are placed on a glass slide at positions of "a3" and "c2," respectively (Figure 4d). The sensor skin is brought in contact with the objects (5 mm compression distance). Figure 4e-i,ii shows the strain and pressure sensors' direct responses in a 4 × 4 matrix while Figure 4e-iii,iv shows the calculated compression and corresponding compliance based on the model presented in Section 3.1. The sensor skin nicely identifies the location and compliance of the PDMS and Ecoflex cylinders with corresponding values of 0.11 and 0.18 mm N^{-1}.

In the second case (Figure 4f), a PDMS cylinder with a radius of 2.2 cm is embedded into an Ecoflex membrane with a 4.5 cm side and 0.8 mm thickness. The testing results and corresponding processing results are displayed in Figure 4g. The average R_s from Ecoflex region is 1.52 Ω and average R_s from PDMS region is 0.66 Ω while the average R_p from Ecoflex region is 1.41 Ω and average R_p from PDMS region is 2.03 Ω. The resulting compliance is 0.11 and 0.15 mm N^{-1} for PDMS and Ecoflex, respectively, which matches the characterization results of the single bimodal

unit. This simple sensor matrix can simultaneously detect contour and position of objects as well as distinct local softer/stiffer regions, suggesting a potential use in smart prosthesis for medical and healthcare manipulation.

4. Conclusion

In this work, we present a soft bimodal sensor system, based on resistive pressure and strain, mounted on rigid robotic hands, enabling the computation of the compliance of any target object. The sensors and interconnects are prepared with spray-coated liquid metal and are embedded in silicone elastomer as substrate/encapsulation material. Liquid metal spray-coating technique not only enables scalable manufacturing of liquid metal devices, but also supports the processing of liquid metal vias. Thanks to this technique, a double-sided LM patterning technique is achieved to reliably separate the sensing and wiring layers, making the system more compact. The soft liquid metal does not restrict the sensor deformation thereby enabling accurate probing of soft matter.

With this sensor system, our main emphasis is on the interaction between the soft sensor and an object of undetermined softness, and this contact influences the sensors' readings. We first investigated how the target material and sensor carrier material influence the soft resistive sensors for pressure and strain detection by simulation to prove the idea. Then we established a mechanical model to study the working principle of the two sensors' combination to quantify compliance. After that, mounted on a robotic palm or finger, the soft bimodal sensors were tested with known objects (commercial rubber, PDMS, Ecoflex, and hydrogel) and unknown objects (chick breast and chick heart) to verify the algorithm. In addition, a compliance sensor matrix is demonstrated to perform the compliance mapping over a larger area, which demonstrates its potential applications in robotics or prosthetics.

The softness sensing system presented in this study allows to accurately determine the softness of an object across a broad range. However, there are several limitations that warrant future research.

First, both the sensor and the object under test need to be relatively flat. A curved sensor alters the contact profile, affecting not only the sensor's readings but also necessitating adjustments to the mechanical model and corresponding algorithms. Similarly, the object being tested must also be flat, as a curved surface compromises the integrity of the softness sensing method. Future work will explore solutions such as incorporating strain sensor rosettes to monitor bending states and miniaturizing the sensor to facilitate localized flat contact with the target object.

Second, the object being tested must be of sufficient thickness to ensure that the shape and rigidity of the underlying testing platform do not influence the results.

Lastly, further investigation is needed in the area of contact between two viscoelastic materials. Integrating more kinematic sensors—such as velocity and acceleration sensors or Inertial Measurement Units (IMUs)—with strain/stress sensors could lead to more dynamic characterizations and measurements. The application of advanced mechanical models and cutting-edge data processing techniques, like machine learning and artificial intelligence, could also significantly contribute to advancements in multisensor integration.

The primary aim of this study is to shed light on the challenges involved in sensor–object softness interactions, while proposing a relatively straightforward design for bimodal sensing units that are compatible with existing robotic manipulators and hands. Achieving a realistic mimicry of human skin perception, however, will necessitate further research in various domains, including contact mechanics, sensing mechanisms, device design, and distributed sensing computation.

The main focus of this work is to highlight the challenge associated with sensor–object softness interaction and propose a relatively simple design of bimodal sensing units compatible with current robotic manipulators and hands. A realistic bionic human skin perception ability will, however, require further in the areas of contact mechanics, sensing mechanisms, device design, and distributed sensing computation.

5. Experimental Section

DSLM Patterning: An illustration of the fabrication process is presented in Figure S1, Supporting Information. A glass wafer carrier was spin-coated with a 200 µm thick layer of Ecoflex (Ecoflex 0030, Smooth-on, Inc.) as an adhesive layer. A 23 µm thick polyethylene terephthalate (PET, Mylar 23A, Lohmann Technologies), shown as bottom PET in Figure S1 in the Supporting Information, was placed on the Ecoflex flatly. Next a 100 µm thick Ecoflex film was spin-coated and covered with another 23 µm thick PET (top PET) stencil shadow mask. Then the PET/Ecoflex/PET stack was removed from the glass/Ecoflex to be a freestanding multilayer. The stack was laser-patterned (MM200-USP, Optec Laser Micromaching Systems) with the desired features to create the vias and patterns of the sensors. EGaIn was then spray coated (Conformal coating tool, Nordson Asymtec) to fill the vias and the pattern of the resistive sensors with the thickness of 20 µm of liquid metal. The spray coating enabled a high patterning resolution of 20 µm (Figure S8, Supporting Information). After removing the top PET, a 200 µm thick Ecoflex membrane was spin-coated to encapsulate the sensor matrix.

For the patterning of the other surface, the stack was flipped over and put on another glass wafer based on the adhesion from the Ecoflex itself. After the alignment, the second layer was laser-patterned to get the pattern for the wiring. Followed by another time of EGaIn spray coating, the pattern of LM of wiring was completed on the other surface, connected with the sensor layer by the vias. In the end, the LM wiring layer was connected to the external conductive wires and then encapsulated by Ecoflex.

Characterization Setup: The device was attached onto a 3D-printed block screw-mounted on an Electromechanical Universal Test System (UTS, C42.503, MTS Systems), while the different target objects were placed below the device, as shown in Figure 3a. The top block moved toward the bottom target object at a constant velocity rate (5% s^{-1}). The electrical resistance was measured with a two-point probe setup (2400 source-meter, Keithley) at 6 Hz with a dedicated LabVIEW program.

Hydrogel Preparation: Agarose powder (Agarose DNA Grade (100 bp to 23 kb), Electran for electrophoresis) was diluted with deionized water (0.5 wt%) while heated on a hot plate until the solution became clear. The agarose solution was poured into a negative mold and cooled down until the hydrogel was fully solidified. The fabricated hydrogel phantom was kept in a refrigerator at 3 °C overnight before used.

Supporting Information

Supporting Information is available from the Wiley Online Library or from the author.

Acknowledgements

The authors acknowledge support from the Bertarelli Foundation and the SNSF NCCR Robotics for their financial support. The authors thank A. Guillet, V. Ruhaut, and M. Stoeckel (Neuronal Microsystems Platform, Foundation Campus Biotech Geneva (FCBG) for guidance with the microfabrication facilities.

Open access funding provided by Ecole Polytechnique Federale de Lausanne.

Conflict of Interest

The authors declare no conflict of interest.

Data Availability Statement

The data that support the findings of this study are available from the corresponding author upon reasonable request.

Keywords

electronic skin, liquid metal film, mechanical sensing, robotics, softness

Received: July 26, 2023
Revised: September 21, 2023
Published online:

[1] *Pervasive Haptics*, (Eds: H. Kajimoto, S. Saga, M. Konyo), Springer, Tokyo, Japan **2016**.
[2] R. L. Klatzky, D. Pawluk, A. Peer, *Proc. IEEE* **2013**, *101*, 2081.
[3] R. D. Howe, W. J. Peine, D. A. Kantarinis, J. S. Son, *IEEE Eng. Med. Biol. Mag.* **1995**, *14*, 318.
[4] M. Santello, M. Bianchi, M. Gabiccini, E. Ricciardi, G. Salvietti, D. Prattichizzo, M. Ernst, A. Moscatelli, H. Jörntell, A. M. L. Kappers, K. Kyriakopoulos, A. Albu-Schäffer, C. Castellini, A. Bicchi, *Phys. Life Rev.* **2016**, *17*, 1.
[5] M. A. Srinivasan, R. H. Lamotte, *J. Neurophysiol.* **1995**, *73*, 88.
[6] R. M. Friedman, K. D. Hester, B. G. Green, R. H. Lamotte, *Exp. Brain Res.* **2008**, *191*, 133.
[7] C. Pacchierotti, S. Sinclair, M. Solazzi, A. Frisoli, V. Hayward, D. Prattichizzo, *IEEE Trans. Haptics* **2017**, *10*, 580.
[8] R. S. Dahiya, G. Metta, M. Valle, G. Sandini, *IEEE Trans. Rob.* **2010**, *26*, 1.
[9] H. Chen, L. Dejace, S. P. Lacour, *Annu Rev Control, Rob. Auton. Syst.* **2021**, *4*, 629.
[10] H. A. U. K. Chung, A. Y. Rwei, A. Hourlier-Fargette, S. Xu, K. Lee, E. C. Dunne, Z. Xie, C. Liu, A. Carlini, D. H. Kim, D. Ryu, E. Kulikova, J. Cao, I. C. Odland, K B. Fields, B. Hopkins, A. Banks, C. Ogle, D. Grande, J. B. Park, J. Kim, M. Irie, H. Jang, J. Lee, Y. Park, J. Kim, H. H. Jo, H. Hahm, R. Avila, Y. Xu, et al., *Nat. Med.* **2020**, *26*, 418.
[11] A. Miyamoto, S. Lee, N. F. Cooray, S. Lee, M. Mori, N. Matsuhisa, H. Jin, L. Yoda, T. Yokota, A. Itoh, M. Sekino, H. Kawasaki, T. Ebihara, M. Amagai, T. Someya, *Nat. Nanotechnol.* **2017**, *12*, 907.
[12] M. Han, L. Chen, K. Aras, C. Liang, X. Chen, H. Zhao, K. Li, N. R. Faye, B. Sun, J.-H. Kim, W. Bai, Q. Yang, Y. Ma, W. Lu, E. Song, J. M. Baek, Y. Lee, C. Liu, J B. Model, G. Yang, R. Ghaffari, Y. Huang, I. R. Efimov, J. A. Rogers, *Nat. Biomed. Eng.* **2020**, *4*, 997.
[13] S. Raspopovic, M. Capogrosso, F. M. Petrini, M. Bonizzato, J. Rigosa, G. Di Pino, J. Carpaneto, M. Controzzi, T. Boretius, E. Fernandez, G. Granata, C. M. Oddo, L. Citi, A. L. Ciancio, C. Cipriani, M. C. Carrozza, W. Jensen, E. Guglielmelli, T. Stieglitz, P. M. Rossini, S. Micera, *Sci. Transl. Med.* **2014**, *6*, 222ra19.
[14] J. W. Kwak, M. Han, Z. Xie, H. A. U. K. Chung, J. Y. Lee, R. Avila, J. Yohay, X. Chen, C. Liang, M. Patel, I. Jung, J. Kim, M. Namkoong, K. Kwon, X. U. Guo, C. Ogle, D. Grande, D. Ryu, D. H. Kim, S. Madhvapathy, C. Liu, D. A. S Yang, Y. Park, R. Caldwell, A. Banks, S. Xu, Y. Huang, S. Fatone, J. A. Rogers, *Sci. Transl. Med.* **2020**, *12*, eabc4327.
[15] L. Dejace, N. Laubeuf, I. Furfaro, S. P. Lacour, *Adv. Intell. Syst.* **2019**, *1*, 1900079.
[16] K. K. Kim, Y. Suh, S. H. Ko, *Adv. Intell. Syst.* **2021**, *3*, 2000157.
[17] M D. Dickey, *Adv. Mater.* **2017**, *29*, 1606425.
[18] S. Wang, J. Xu, W. Wang, G.-J. N. Wang, R. Rastak, F. Molina-Lopez, J. W. Chung, S. Niu, V. R. Feig, J. Lopez, T. Lei, S.-K. Kwon, Y. Kim, A. M. Foudeh, A. Ehrlich, A. Gasperini, Y. Yun, B. Murmann, J. B.-H. Tok, Z. Bao, *Nature* **2018**, *555*, 83.
[19] Y. Jiang, Z. Zhang, Y.-X. Wang, D. Li, C.-T. Coen, E. Hwaun, G. Chen, H.-C. Wu, D. Zhong, S. Niu, W. Wang, A. Saberi, J.-C. Lai, Y. Wu, Y. Wang, A. A. Trotsyuk, K. Y. Loh, C.-C. Shih, W. Xu, K. Liang, K. Zhang, Y. Bai, G. Gurusankar, W. Hu, W. Jia, Z. Cheng, R. H. Dauskardt, G. C. Gurtner, J. B.-H. Tok, K. Deisseroth, et al., *Science* **2022**, *375*, 1411.
[20] N. Matsuhisa, X. Chen, Z. Bao, T. Someya, *Chem. Soc. Rev.* **2019**, *48*, 2946.
[21] K. Jang, K. Li, H. A. U. K. Chung, S. Xu, H. N. A. Jung, Y. Yang, J. W. Kwak, H. H. Jung, J. Song, C. Yang, A. Wang, Z. Liu, J. Y. Lee, B. H. Kim, J.-H. Kim, J. Lee, Y. Yu, B. J. Kim, H. Jang, K. I. J. Yu, J. Kim, J. W. Lee, J.-W. Jeong, Y. M. Song, Y. Huang, Y. Zhang, J A. Rogers, *Nat. Commun.* **2017**, *8*, 15894.
[22] Z. Yan, F. Zhang, J. Wang, F. Liu, X. Guo, K. Nan, Q. Lin, M. Gao, D. Xiao, Y. Shi, Y. Qiu, H. Luan, J. H. Kim, Y. Wang, H. Luo, M. Han, Y. Huang, Y. Zhang, J A. Rogers, *Adv. Funct. Mater.* **2016**, *26*, 2629.
[23] S. P. Lacour, G. Courtine, J. Guck, *Nat. Rev. Mater.* **2016**, *1*, 16063.
[24] I. R. Minev, P. Musienko, A. Hirsch, Q. Barraud, N. Wenger, E. M. Moraud, J. Gandar, M. Capogrosso, T. Milekovic, L. Asboth, R. F. Torres, N. Vachicouras, Q. Liu, N. Pavlova, S. Duis, A. Larmagnac, J. Vörös, S. Micera, Z. Suo, G. Courtine, S. P. Lacour, *Science* **2015**, *347*, 159.
[25] G. Cai, J. Wang, K. Qian, J. Chen, S. Li, P. S. Lee, *Adv. Sci.* **2017**, *4*, 1600190.
[26] H. Chen, L. Miao, Z. Su, Y. Song, M. Han, X. Chen, X. Cheng, D. Chen, H. Zhang, *Nano Energy* **2017**, *40*, 65.
[27] B.-U. Hwang, A. Zabeeb, T. Q. Trung, L. Wen, J. D. Lee, Y. Choi, H.-B. Lee, J. H. Kim, J. G. Han, N.-E. Lee, *NPG Asia Mater* **2019**, *11*, 23.
[28] S. Zhao, R. Zhu, *Adv. Mater.* **2017**, *29*, 1606151.
[29] C. Zhu, A. Chortos, Y. Wang, R. Pfattner, T. Lei, A. C. Hinckley, I. Pochorovski, X. Yan, J. W.-F. To, J. Y. Oh, J. B.-H. Tok, Z. Bao, B. Murmann, *Nat. Electron.* **2018**, *1*, 183.
[30] Y. Wu, Q. Huang, J. Nie, J. Liang, N. Joshi, T. Hayasaka, S. Zhao, M. Zhang, X. Wang, L. Lin, *J. Nanosci. Nanotechnol.* **2019**, *19*, 5310.
[31] P.-G. Su, C.-C. Shiu, *Sens. Actuators, B* **2012**, *165*, 151.
[32] Q. Hua, J. Sun, H. Liu, R. Bao, R. Yu, J. Zhai, C. Pan, Z. L. Wang, *Nat. Commun.* **2018**, *9*, 244.
[33] M. Naqi, S. Lee, H.-J. Kwon, M. G. Lee, M. Kim, T. W. Kim, H. K. Shin, S. Kang, S. Gandla, H.-S. Lee, Y. Ahn, S. Lee, S. Kim, *Adv. Mater. Technol.* **2019**, *4*, 1900619.
[34] L. Beker, N. Matsuhisa, I. You, S. R. A. Ruth, S. Niu, A. Foudeh, J. B.-H. Tok, X. Chen, Z. Bao, *Proc. Natl. Acad. Sci. U. S. A.* **2020**, *117*, 11314.
[35] S. Sokhanvar, M. Packirisamy, J. Dargahi, *IEEE Sens. J.* **2009**, *9*, 1679.
[36] H. Zhao, K. O'brien, S. Li, R. F. Shepherd, *Sci. Rob.* **2016**, *1*, eaai7529.